

FOREGROUND PREDICTIONS FOR THE COSMIC MICROWAVE BACKGROUND POWER SPECTRUM FROM MEASUREMENTS OF FAINT INVERTED RADIO SOURCES AT 5 GHz

MICHAEL D. SCHNEIDER

Lawrence Livermore National Laboratory, P.O. Box 808 L-210, Livermore, CA 94551, USA

ROBERT H. BECKER

Department of Physics, University of California, One Shields Avenue, Davis, CA 08991, USA
Lawrence Livermore National Laboratory, P.O. Box 808 L-415, Livermore, CA 94551, USA

WILLEM DE VRIES

Lawrence Livermore National Laboratory, P.O. Box 808 L-211, Livermore, CA 94551, USA

RICHARD L. WHITE

Space Telescope Science Institute, Baltimore, MD 21218, USA
LLNL-JRNL-501091

ABSTRACT

We present measurements of a population of matched radio sources at 1.4 and 5 GHz down to a flux limit of 1.5 mJy in 7 deg² of the NOAO Deep Field South. We find a significant fraction of sources with inverted spectral indices that all have 1.4 GHz fluxes less than 10 mJy and are therefore too faint to have been detected and included in previous radio source count models that are matched at multiple frequencies. Combined with the matched source population at 1.4 and 5 GHz in 1 deg² in the ATESP survey, we update models for the 5 GHz differential number counts and distributions of spectral indices in 5 GHz flux bins that can be used to estimate the unresolved point source contribution to the cosmic microwave background temperature anisotropies. We find a shallower logarithmic slope in the 5 GHz differential counts than in previously published models for fluxes $\lesssim 100$ mJy as well as larger fractions of inverted spectral indices at these fluxes. Because the Planck flux limit for resolved sources is larger than 100 mJy in all channels, our modified number counts yield at most a 10% change in the predicted Poisson contribution to the Planck temperature power spectrum. For a flux cut of 5 mJy with the South Pole Telescope and a flux cut of 20 mJy with the Atacama Cosmology Telescope we predict a $\sim 30\%$ and $\sim 10\%$ increase, respectively, in the radio source Poisson power in the lowest frequency channels of each experiment relative to that predicted by previous models.

Subject headings: cosmic background radiation – cosmological parameters – Cosmology: observations – inflation – surveys

1. INTRODUCTION

A main science driver for ongoing high-resolution cosmic microwave background (CMB) experiments is to measure the amplitude and tilt of the power spectrum of primordial density fluctuations and thereby constrain models of cosmic inflation. On large angular scales (multipoles $\ell \lesssim 1000$), the power spectrum of CMB temperature anisotropies is directly related to the primordial density power spectrum by well-understood baryon physics. However, on smaller angular scales various astrophysical foregrounds dominate the measured temperature power spectrum and obscure the primordial signal.

For frequencies less than about 150 GHz a dominant foreground is the flux from radio-loud galaxies and blazars that is unresolved by the CMB experiment beam and therefore cannot be masked out (Tegmark & Efsthathiou 1996; Knox 1999; Scott & White 1999; Hufenberger et al. 2008; Colombo & Pierpaoli 2010; Milea et al. 2011). Previous radio surveys have identified a significant population of sources from 1 to 30 GHz

that have flat or “inverted” spectral energy distributions (SEDs) such that their flux is roughly constant or increasing with increasing frequency (Guerra et al. 2002; Colombo & Pierpaoli 2010; Prandoni et al. 2010) and are therefore potentially significant foregrounds for CMB observations. Physical models for these objects predict that they are dominated by synchrotron emission from relativistic jets in active galactic nuclei (AGNs; Danese et al. 1987; Toffolatti et al. 1998; de Zotti et al. 2005, 2010; Tucci et al. 2011; Rani et al. 2011) with the large spectral indices determined either by dominant emission from compact optically thick regions of the jet, early or late stages of AGN evolution, or chance variability in the source. Such physical models predict that the SEDs of these sources should break and decline somewhere between tens and hundreds of GHz. The flat and inverted radio sources detected around a few GHz should then contribute negligible flux at millimeter frequency CMB observations (where infrared emission from galactic dust becomes a problem instead).

Thermal synchrotron emission from advection-dominated accretion flows (ADAFs) may be also be a

significant contribution to the low-frequency radio foregrounds in CMB experiments (Perna & Di Matteo 2000; Pierpaoli & Perna 2004; Toffolatti et al. 2005). ADAFs may also show inverted spectra up to several tens of GHz when the emission region is significantly compact. Using the model of Perna & Di Matteo (2000) and considering constraints on the source counts from the Ryle telescope, ATCA, and *Wilkinson Microwave Anisotropy Probe* (*WMAP*) surveys, de Zotti et al. (2005) showed that the predicted differential number counts of ADAFs at 30 GHz are at least two orders of magnitude smaller than the blazar counts for fluxes greater than ~ 1 mJy (see their Figure 14). We therefore only consider SED models for blazars with inverted spectra and neglect any possible (sub-dominant) contribution from ADAF sources.

Aside from CMB power spectrum measurements, radio foregrounds are also a significant foreground for Sunyaev–Zel’dovich measurements of galaxy clusters (Knox et al. 2004; White & Majumdar 2004; de Zotti et al. 2005; Lin et al. 2009; Sehgal et al. 2010; Reese et al. 2011) and for testing for non-Gaussianity in the CMB (Elsner et al. 2010; Curto et al. 2011).

As CMB experiments obtain better resolution, the lower flux limit will decrease for resolving and removing radio sources. It is then important to characterize the radio source number counts and spectral indices at fluxes below the resolved source flux cut to mitigate the contamination from unresolved sources. While *WMAP*¹ was able to remove radio point sources with fluxes greater than 0.7 Jy, Planck² resolves all sources with fluxes greater than ~ 0.2 Jy (Planck Collaboration et al. 2011). The Atacama Cosmology Telescope (ACT)³ and the South Pole Telescope (SPT)⁴ are able to resolve all sources above 20 and 5 mJy respectively (Marriage 2011; Vieira et al. 2010). Existing models for radio source counts and SEDs have largely been calibrated only to a flux limit of 30–100 mJy (de Zotti et al. 2005; Tucci et al. 2011), so the models would have to be extrapolated to lower fluxes in order to analyze these ongoing CMB experiments.

We present measurements of the population of faint radio sources complete to 1.5 mJy at 1.4 and 5 GHz collected with the Very Large Array (VLA) in 7 deg² of the NOAO Deep Field South (DFS). Our sources are matched at the two observation frequencies allowing us to determine the spectral index for each source. To apply our source catalog for predicting the unresolved point source contamination in the CMB, we compare primarily with Tucci et al. (2011) (hereafter T11) who present models for the number counts and SEDs of radio sources calibrated from many different data sets. Our data are new primarily in reaching fainter flux densities with spectral indices of matched sources.

This paper is organized as follows. We describe our observations and the construction of our source catalog in Section 2. We derive new fits to the 5 GHz differential number counts of our sources and the distributions of spectral indices in Section 3.1. We then review SED

models that use the fits to the 5 GHz counts and indices as inputs for extrapolating source fluxes to higher frequencies in Section 3.2. We show the impact of our new data and models on the predicted high-frequency number counts in Section 4.1 and predict the impact on measurements of the Planck temperature–temperature (TT) power spectrum in Section 4.2. We draw conclusions about the impact of faint radio sources on future CMB measurements in Section 5. In Appendix A we describe a statistical model for propagating the errors in the measured fluxes and spectral indices into the estimated high-frequency differential counts and CMB Poisson contribution from unresolved sources. We describe the structure of our new source catalog in Appendix B and present a sample of the measured source fluxes in Table 5. The full catalog is available for download from the VizieR database.

2. SOURCE CATALOG

We present a catalog of 362 new sources discovered with VLA imaging in 7 deg² of the NOAO DFS at 1.4 and 5 GHz (see Appendix B for a sample of the catalog). The data reduction and catalog construction were performed with the same methods as in the Faint Images of the Radio Sky at Twenty cm (FIRST) survey (White et al. 1997). The survey has a resolution of 5 arcsec at both frequencies. We include in our catalog only sources that are matched in the two bands. There are 700 identified sources in the field at 1.4 GHz, so roughly half of the sources are matched at 5 GHz to give us our 362 sources. There are seven point sources in our 5 GHz catalog that are not matched at 1.4 GHz. All seven sources have 5 GHz fluxes between 1 and 5 mJy, and therefore likely have inverted spectral indices such that the 1.4 GHz flux is below the FIRST survey detection threshold around 1 mJy. Lacking spectral index measurements for these seven sources, we do not include them in our subsequent analysis. However, all our results must be interpreted remembering that there are likely more inverted sources near our flux limit that would further boost the differential number counts of faint point sources.

The ATESP (Prandoni et al. 2000; Prandoni et al. 2006) catalog has a similar resolution to ours and has 118 matched sources in the same frequency bands over 1 deg². The ATESP catalog is complete below 1 mJy and is therefore a useful complement to our catalog. We will consider both the NOAO DFS and ATESP catalogs in tandem when fitting models for the differential number counts and SEDs of the 5 GHz source population.

The observed fluxes and the inferred spectral indices (defined by the relation $S \propto \nu^\alpha$ where S is the flux, ν is the frequency, and α is the spectral index) for each of our matched sources are shown in Figure 1. There are 28 and 9 sources with spectral indices $\alpha_{1.4-5} > 0.3$ in the NOAO DFS and ATESP catalogs respectively, which we label as “inverted” spectrum sources (following a common convention). All of our inverted spectrum sources have 1.4 GHz fluxes < 10 mJy so they would not have been identified in earlier surveys with larger flux limits. The sources with $-0.5 < \alpha_{1.4-5} \leq 0.3$ (129 in the NOAO DFS catalog and 55 in the ATESP catalog) are labeled as “flat-spectrum” and could also potentially be visible at higher frequencies. Again, we see in the top panels of Figure 1 that the majority of our flat-spectrum

¹ <http://map.gsfc.nasa.gov>

² <http://www.esa.int/planck>

³ <http://www.physics.princeton.edu/act/>

⁴ <http://pole.uchicago.edu>

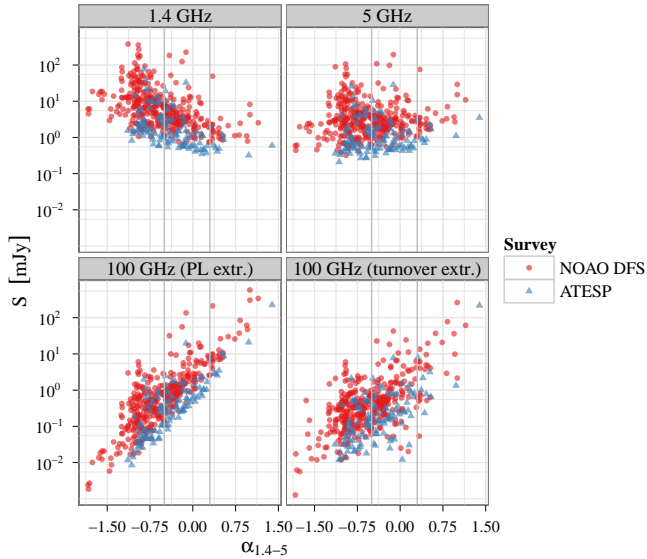


Figure 1. Flux in the observation bands of 1.4 and 5 GHz vs. the spectral index inferred from these bands. The bottom panels show the fluxes extrapolated to 100 GHz using two different SED models as described in Section 3.2. The bottom left panel uses a simple power-law (PL) model while the bottom right panel uses a model from T11 that has a “turnover” in the SED at $\sim 10 - 30$ GHz.

sources have 1.4 GHz fluxes below 10 mJy. As a preliminary illustration of the potential contribution of these source populations for high-frequency number counts we show the extrapolated fluxes of our sources at 100 GHz using two different SED models in the bottom panels of Figure 1. We will explain the SED models in the next section, but note here that with both a “power-law” (PL) SED model and an SED model with a break or “turnover” many of our sources are predicted to have 100 GHz fluxes greater than 1 mJy and will therefore be detectable in high-resolution CMB experiments. In our fits to the 5 GHz differential number counts in the next section, it will also be important to note that there is not a strong correlation between the 5 GHz flux and $\alpha_{1.4-5}$ in Figure 1.

In Figure 2 we show the differential number counts at 1.4 GHz estimated from the NOAO DFS and ATESP catalogs and compare with the fit to the number counts published by Tegmark & Efstathiou (1996) from the FIRST survey at 1.4 GHz (White et al. 1997), which is claimed to be complete to $S = 0.75$ mJy. Both the NOAO DFS and ATESP data match the fit well for $S \gtrsim 10$ mJy but the NOAO DFS data clearly give fewer number counts for $S \lesssim 3$ mJy while the ATESP counts drop below the fit for $S \lesssim 1$ mJy. The incompleteness at low flux in both catalogs is primarily caused by the requirement to match sources at 5 GHz, which omits steep-spectrum-sources at 1.4 GHz that are not detected at 5 GHz. This selection effect is apparent in the top left panel of Figure 1 where the minimum flux for steep-spectrum sources ($\alpha_{1.4-5} < -0.5$) is much larger than that for flat+inverted sources.

3. MODELS FOR SOURCE COUNTS AND SPECTRAL ENERGY DISTRIBUTIONS

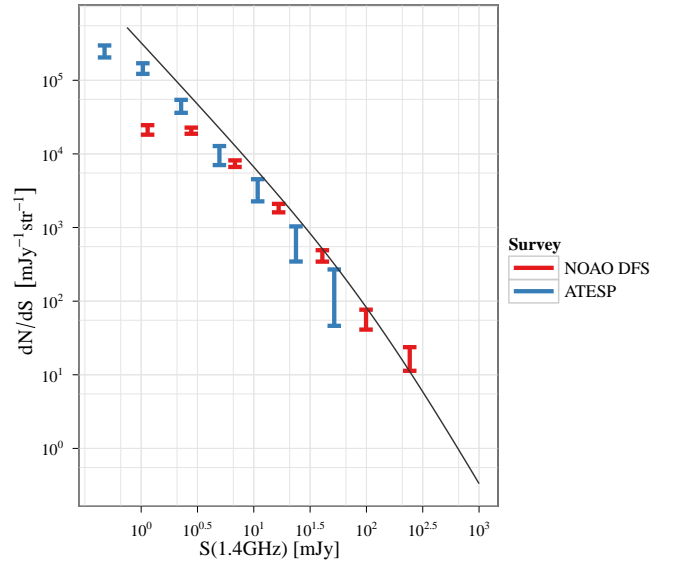


Figure 2. Estimated differential number counts at 1.4 GHz. The solid line is the fit to the counts from the VLA FIRST survey at 1.5 GHz from Tegmark & Efstathiou (1996), which is complete to 0.75 mJy.

In this section, we describe the modifications based on our data to the T11 models for 5 GHz number counts, spectral index distributions, and SEDs used for extrapolation of the counts to higher frequencies. The key changes to the T11 model are from the extension to lower 5 GHz fluxes.

3.1. Models for 5 GHz Sources

We adopt the form of the fit function from Equation (1) of T11 for the 5 GHz differential number counts for flat+inverted spectrum sources,

$$\frac{dN_{\text{flat+inv}}}{dS_5} = n_{0,f} \frac{(S/S_{0,f})^{k_f}}{1 - e^{-1}} \left(1 - e^{-(S/S_{0,f})^{\ell_f - k_f}} \right). \quad (1)$$

T11 found best fit parameters $n_{0,f} = 47.4 \text{ Jy}^{-1} \text{sr}^{-1}$, $S_{0,f} = 1.67 \text{ Jy}$, $k_f = 0.50$ and $\ell_f = -0.66$. Because of the small areas covered by the NOAO DFS and ATESP catalogs, we do not have good statistics for constraining the differential number counts at fluxes greater than about 100 mJy. We therefore include the differential count estimates (covering $0.1 \lesssim S \lesssim 10 \text{ Jy}$) presented in the right panel of Figure 2 of T11 when deriving new best fit parameters for the fitting function in Equation (1). In T11, the steep-spectrum number counts are defined as the difference between the dN/dS_5 model of Toffolatti et al. (1998) and Equation (1). Here, we introduce a fit function for the steep-spectrum counts that can be used to fit our steep-spectrum sources,

$$\frac{dN_{\text{st}}}{dS_5} = n_{0,s} \frac{(S/S_{0,s})^{k_s}}{1 - e^{-1}} \left(1 - e^{-(S/S_{0,s})^{\ell_s - k_s}} \right) + n_{1,s} \left(\frac{S}{1 \text{ Jy}} \right)^{a_1}, \quad (2)$$

where $n_{0,s} = 88 \text{ Jy}^{-1} \text{sr}^{-1}$, $S_{0,s} = 0.12 \text{ Jy}$, $k_s = 0.84$, $\ell_s = -0.49$, $n_{1,s} = 10.9 \text{ Jy}^{-1} \text{sr}^{-1}$, and $a_1 = 0.33$ fit the steep-spectrum count model reported in T11.

When fitting to the differential counts estimated from

our catalogs, we multiply Equations (1) and (2) by selection functions of the form,

$$\phi(S_5; S_{\min}, a) \equiv 1 - e^{-(S_5/S_{\min})^a}, \quad (3)$$

to account for incomplete source extraction near the limiting fluxes in each catalog. We fit separate values of S_{\min} and a for the NOAO DFS and ATESP catalogs. For each catalog, we also fit separate S_{\min} and a values for the flat+inverted and steep-spectrum samples because the flux limit of matched sources is a function of the source spectral index (see, e.g., the skewed lower bounds of the scatter plots in the top panels of Figure 1).

We fit new values for the flat+inverted differential number count model in Equation (1) with the following procedure.

1. We create separate histograms for the 5 GHz fluxes in the NOAO DFS and ATESP catalogs with the optimal histogram bins chosen as prescribed by Hogg (2008) (assuming the logarithm of the bin widths is constant). The histogram bin values with Poisson uncertainties are our estimators for the 5 GHz differential number counts.
2. We combine our number count estimates with those presented in the right panel of Figure 2 in T11, which compares the 5 GHz count estimates from a number of surveys covering the flux range ~ 100 mJy to ~ 10 Jy. Because our data cover a small area, we do not have good estimates of the number counts above ~ 100 mJy so the data from T11 is essential to constrain the “bend” and high-flux slope of the fit function in Equation (1). Note that we assign new Poisson uncertainties to the data points extracted from Figure 2 in T11 according to the number of sources in each flux bin (derived according to the area of each survey). The uncertainties assigned to our differential count estimates and those from T11 are therefore consistent.
3. We extract samples from the joint posterior of all the fit parameters in Equation (1) and S_{\min} and a (from Equation (3)) for each of the NOAO DFS and ATESP data sets using Markov Chain Monte Carlo (MCMC) with a likelihood given by the product of the Poisson likelihoods for each count estimate in each flux bin for each data set (our two catalogs and those from Figure 2 in T11). We thin the MCMC samples to obtain uncorrelated samples of the joint parameter posterior.
4. We define the best fit parameters as the medians of the marginal posteriors for each parameter.

Using this algorithm, the new fit parameters for Equation (1) are, $k_f = 0.438 \pm 0.0142$, $n_0 = 46.7 \pm 1.49$ Jy $^{-1}$ sr $^{-1}$, $\ell = -0.755 \pm 0.137$, and $S_0 = 2.31 \pm 0.222$ Jy. Note in particular that the addition of our data favors a much smaller value of k_f than the value of $k_f = 0.5$ presented in T11, which implies a larger number density of faint sources than would be inferred by extrapolating the T11 fits to faint fluxes. The logarithm of the ratio of likelihoods for our best fit parameters and those of T11 is 23.6, indicating that our new fit is favored by the data with strong significance. The selection function

minimum flux fits are $S_{\min} = 1.48$ for the NOAO DFS catalog and $S_{\min} = 0.405$ for the ATESP catalog. We use these fits to determine the minimum flux values when creating simulated source catalogs in Section 3.2.

We adopt a simpler maximum-likelihood procedure to fit the steep-spectrum count parameters defined in Equation (2) for three reasons: (1) the steep-spectrum sources presented in the left panel of Figure 2 in T11 have much larger uncertainties for constraining the fit function, (2) our data turns out to be entirely consistent with the fit function parameters derived from the T11 results, and (3) the steep-spectrum number counts are not important for predicting the higher frequency counts at the CMB frequencies we are considering in this paper. The bottom panel in Figure 3 illustrates how our data are consistent with the T11 result.

The distributions of spectral indices in 5 GHz flux bins are shown in Figure 4. We make the simplifying assumption that the spectral index is statistically independent of the 5 GHz flux, which is consistent with Figure 1. We again follow T11 and fit the histograms with separate truncated distributions for flat+inverted ($\alpha > -0.5$) and steep ($\alpha \leq -0.5$) spectral types (shown by the red solid lines in Figure 4). The dashed black lines in the figure show the fits from T11 for their lowest-flux bin, $100 < S/\text{mJy} < 158$. We find the distributions are best fit by a mixture of two truncated Gaussian distributions, except for the highest-flux steep-source distribution, which is well fitted by a single truncated Gaussian. The parameters of the fits in Figure 4 are given in Table 1 along with uncertainties on the fit parameters derived from the 68% conditional uncertainty interval on the mean of the largest-index Gaussian fit in each panel of Figure 4. In detail, we calculate uncertainties via bootstrap resampling of each catalog, where we also sample the number of catalog entries from a Poisson distribution and then sample with replacement the catalog entries. We then fit double or single Gaussians to each sub-sample shown in Figure 4, rank order the fitted Gaussian means, or the larger of the two means when two Gaussians are fit, and select the 68% confidence intervals from the ordered samples. We focus on the Gaussian means to understand the possible variation (including Poisson uncertainties) in the inverted spectral index distributions.

It is notable for extrapolating fluxes that our best fit distributions for the flat+inverted spectrum sources have larger tails with positive spectral indices than the T11 fits in their lowest flux bin.

Note that while T11 consider how source variability can change the inferred spectral indices, their modeling shows that variability has only a small effect on the spectral index histograms. We therefore ignore the effect of variability here.

3.2. Flux Extrapolation

We will primarily use the T11 SED models for extrapolating the 5GHz fluxes to higher frequencies (which we will refer to as the “Tucci SED” model). T11 considered both many different data sets with spectral index information as well as physical models for the frequency dependence of the synchrotron emission from the flat-spectrum sources to construct statistical SED models that are consistent with observed differential number

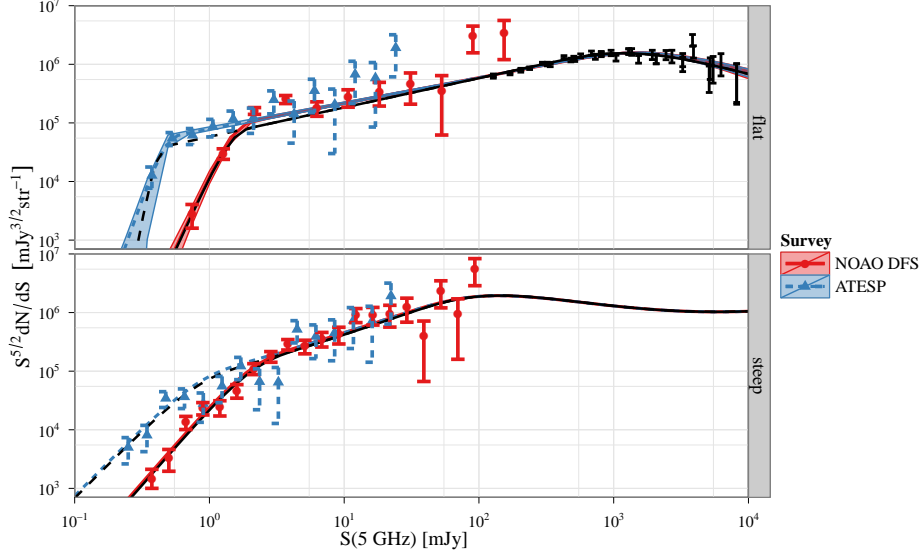


Figure 3. Observed differential number counts at 5 GHz and fits for the flat+inverted spectrum (top) and steep-spectrum (bottom) sources. The red solid lines in each panel are the fits to the NOAO DFS counts (red points and error bars) while the blue dashed lines are the fits to the ATESP counts (blue triangles and error bars). The solid and long-dashed black lines show the fits from Tucci et al. (2011) for the NOAO DFS and ATESP selection functions, respectively. For all data points, the error bars show the 68% confidence intervals assuming the counts in each flux bin are Poisson distributed.

Table 1
Fit Parameters for Spectral Index Distributions

Spectral type	Flux Bin (mJy)	Mean 1	Mean 2	Std. Dev. 1	Std. Dev. 2	Weight
flat+inverted	(0.4,3]	$-0.29^{+0.312}_{-0.314}$	$0.183^{+0.257}_{-0.149}$	$0.112^{+0.105}_{-0.116}$	$0.295^{+0.25}_{-0.313}$	$0.487^{+0.556}_{-0.479}$
flat+inverted	(3,100]	$-0.262^{+0.234}_{-0.411}$	$0.428^{+0.751}_{-0.133}$	$0.176^{+0.207}_{-0.0597}$	$0.46^{+0.355}_{-0.462}$	$0.674^{+0.806}_{-0.41}$
steep	(0.4,3]	$-1.53^{+1.4}_{-1.59}$	$-0.822^{+0.795}_{-0.844}$	$0.185^{+0.178}_{-0.174}$...	$0.092^{+0.13}_{-0.0983}$
steep	(3,100]	$-0.849^{+0.835}_{-0.868}$...	$0.186^{+0.191}_{-0.185}$

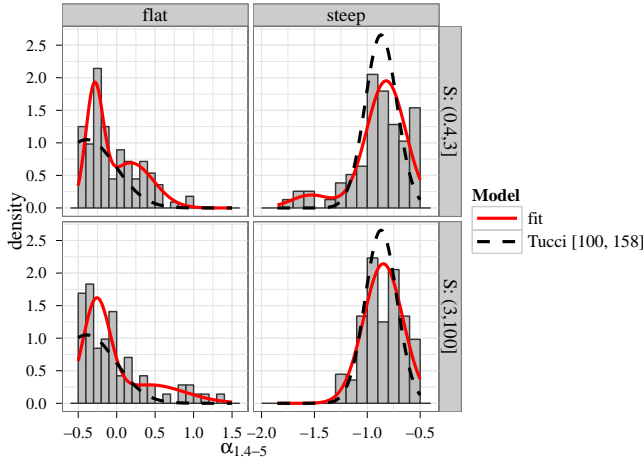


Figure 4. Distribution of spectral indices for flat+inverted (left) and steep-spectrum (right) sources in two 5 GHz flux bins (top and bottom rows) measured from the combined catalogs of the NOAO DFS and ATESP fields. The flux bin ranges in the row side panels are in mJy. The black dashed lines show the fits from T11 in their [100, 158] mJy flux bin, which is the lowest flux bin they consider.

counts at frequencies from 5 to several hundred GHz. We will show in this section that our modified fits to the 5GHz flat+inverted differential counts and the spectral index distributions for fluxes less than 100 mJy further improve the fits of the extrapolated differential number counts at low fluxes with external data sets.

The Tucci SED model assumes that steep-spectrum sources follow a PL SED ($S \propto \nu^\alpha$) with spectral indices $\alpha_{1.4-5} - \Delta\alpha$ and $\Delta\alpha$ Gaussian distributed to model observed steepening at higher frequencies (see Equation (9) in T11). In the description of the steep-spectrum SED, T11 state that, “A small percentage of flattening or upturning sources is also included.” We find that we can reproduce their plots of extrapolated steep-spectrum source counts by assigning 2% of our steep-spectrum sources to have spectral indices drawn from a Gaussian distribution with mean -0.3 and standard deviation 0.2 .

We adopt the “C2Ex” model from T11 for flat-spectrum sources ($-0.5 < \alpha_{1.4-5} < 0.3$) that determines the distribution of break frequencies according to a physical model of the size of the optically thick synchrotron emitting region in FSRQ and BL Lac sources. The model requires knowledge of the redshift distributions of the sources of each type as well as the distributions of Doppler factors that adjust the predicted

flux from a homogeneous spherically symmetric model to model an asymmetric jet. Our sample of faint flat-spectrum sources almost certainly has a different redshift distribution than that assumed by T11 for their high-frequency predictions. This is because for a homogeneous source sample, fainter fluxes imply higher redshifts, while at fixed redshift fainter fluxes imply sources at different evolutionary stage that will again have different redshift distributions. However, in the absence of further information about our catalogs, we simply use the same distributions for the flat-spectrum break frequencies as T11 (shown in Figure 7 of T11). This is probably not a terrible approximation because the distributions of the break frequencies span several orders of magnitude with the mean following a simple scaling with 5 GHz flux and the width determined largely by the assumed size of the emitting region. So modifications in the assumed redshift distribution would yield only minor corrections in the final predicted number counts.

For inverted spectrum sources ($\alpha_{1.4-5} > 0.3$) T11 use the model,

$$S(\nu, \theta) = S_0 \left(\frac{\nu}{\nu_0} \right)^\alpha \left(1 - e^{-\left(\frac{\nu}{\nu_0}\right)^{1-\alpha}} \right), \quad (4)$$

where

$$l \sim -A(l - l_0) \exp \left[-\frac{1}{2} \frac{(l - l_0)^2}{\sigma_l^2} \right], \quad (5)$$

with $l_0 = -0.1$ and $\sigma_l = 0.53$ (see Figure 9 in T11). Note that l is therefore defined with support $[-\infty, l_0]$ and l_0 must be less than 0. The parameter ν_0 in Equation (4) is determined from the distribution of peak frequencies in Table 3 of T11. Again we adopt the distribution for l from T11 without modification.

The T11 SED model as applied in this paper has two main drawbacks. First, the model requires specification of both the distributions of “break” frequencies where the SEDs of inverted and flat-spectrum sources turn over as the radio emission probes different physical regions of the source and of the distributions of the spectral indices after the break. Second, and somewhat related, the T11 SED model has a large number of parameters with unspecified uncertainties so that it is difficult to quantify our confidence in the extrapolated number counts predicted with this model. For comparison then, we also consider the physically unrealistic but simple PL SED model,

$$\bar{S}(\nu; S_0, \alpha) = S_0 \left(\frac{\nu}{\nu_0} \right)^\alpha, \quad (6)$$

with $\nu_0 = 5$ GHz. The PL model will overpredict the number counts at frequencies larger than the typical break frequencies for a given source type. But, the PL model has the advantage that we can easily propagate our uncertainty in the SED model parameters, S_0 and α , into the extrapolated number count predictions and therefore gain some understanding about the relative uncertainties in the number counts from the errors in the data versus the SED model.

We propagate the uncertainty in the PL SED model by computing the marginal posterior probability distribution for the extrapolated flux of each source marginal-

izing over the SED parameters, S_0 and α , and incorporating observational uncertainties in the flux likelihood model. We describe the details of this extrapolation method in Appendix A. The marginal posterior probability for the extrapolated flux allows for full uncertainty propagation and therefore robust foreground removal (conditioned on the choice of SED model). Such a procedure becomes less useful when the available source catalog is an incomplete sample of the population of sources contributing to the foregrounds and when there are many SED parameters to marginalize over leading to large marginal uncertainties. Our catalogs unfortunately meet the former condition because of the relatively small fraction of the sky covered (leading to a dearth of high-flux sources observed) and the Tucci SED model likely meets the latter condition.

Putting aside the incompleteness of our catalogs for fluxes $\gtrsim 100$ mJy, we predict the high-frequency number counts with the PL SED model using the complete error propagation methods of Appendix A. Assuming a log-Normal likelihood for the observed fluxes, the marginal posteriors for the extrapolated fluxes can be computed analytically (and therefore quickly). The resulting extrapolated flux confidence intervals can be used as indicators of the extrapolation error when the SED model is well-constrained.

However, with the many parameters in the Tucci SED model that, upon marginalization, further contribute to the extrapolated flux uncertainties, we instead use the T11 flux extrapolation method to study the impact of our new data on the “central” extrapolated count predictions. In T11 the differential number counts at high frequencies are predicted by first simulating a source catalog by sampling sources from the fits to the 5 GHz differential counts and sampling spectral indices from the fits to the 5 GHz spectral index histograms, and then plugging the sampled values into the SED models for each spectral class. The extrapolated simulated fluxes can be histogrammed to estimate the high-frequency number counts in the same way that the observed low-frequency number counts were estimated. Because the predictions from any one simulated catalog can be subject to random fluctuations (mostly at high fluxes where the counts are low) we generate predictions for the Tucci SED model by simulating 10 catalogs with 10^6 sources each and then computing the medians of any summary statistics of the extrapolated catalogs.

4. HIGH-FREQUENCY PREDICTIONS

We now apply the flux extrapolation methods described in Section 3.2 to predict the high-frequency differential number counts and Poisson contributions to the CMB power spectrum. We consider two sets of simulated catalogs for generating predictions with the Tucci SED model. First we simulate catalogs with exactly the same parameters as in T11 (labeled “Tucci et al. 2011” in the figures) but with a lower flux limit of 0.4 mJy, which is where our fit to the ATESP selection function (see Equation (3)) has a value of 0.5. To reach this flux limit we unfairly apply the spectral index distributions from T11 for the flux bin [100,158] mJy to all lower fluxes. Our second set of catalogs (labeled “This work” in the figures) uses the modified dN/dS fit with $k_f = 0.438$ for flat+inverted sources as found in Figure 3 and the spectral index distri-

butions fit in Figure 4 to simulate the spectral indices of sources with fluxes lower than the lower limit of 100 mJy in T11. As described in Section 3.2, we use the T11 models for both our simulated catalogs for the flat and inverted spectrum break frequencies and high-frequency spectral indices.

4.1. Extrapolated Number Counts

To validate the differential counts model based on our catalogs we first compare with the measured differential counts at 15.7 GHz in the 9C and 10C surveys (AMI Consortium et al. 2011) in Figure 5. The combined 10C survey covers 12 deg² to a flux limit of 0.5 mJy while the 9C survey data cover several hundred square degrees to a limit of 10 mJy. While this provides excellent statistics for the estimates of the differential number counts, the surveys only have a resolution of 30 arcsec compared to our catalogs that have a resolution of 5 arcsec. It is therefore possible that the number of sources observed with 30 arcsec resolution is artificially reduced relative to our model because resolved sources at 5 arcsec are merged together when they happen to fall close together in projection on the sky. Out of the 362 sources in our NOAO DFS catalog, we find 29 source pairs that lie within 30 arcsec of each other and 10 source triplets within a circle of 30 arcsec diameter. To predict the 15.7 GHz differential counts for 30 arcsec resolution we randomly choose sources to merge in our simulated catalogs so that the fractions of merged pairs and triplets match those in the NOAO DFS catalog. Because of low statistics we have made no attempt to choose sources to merge based on any other criteria than random selection. The resulting predicted number counts are shown by the solid blue line labeled “This work, low-res” in Figure 5. Our model is a much better match to the 10C survey number counts than either the T11 model or the de Zotti et al. (2005) model for fluxes less than 8 mJy. The better fit at faint fluxes is mostly due to the increased 5 GHz counts from the fit we found in Figure 3. For the fluxes from 10 mJy to 60 mJy the 9C survey number counts fall well below all of the model predictions, while all the models are in good agreement with the observed counts for larger fluxes.

In Figure 6 we recreate Figure 12 from T11 to compare our predicted differential number counts at 30 GHz with several other surveys. The steep-spectrum sources are a small but non-negligible contribution to the number counts at 30 GHz. The new fit to the low-flux slope of the 5 GHz differential counts in Figure 3 and the larger values of the spectral indices shown in Figure 4 lead to a significant difference in the total 30 GHz counts for fluxes between 1 and ~ 50 mJy. Our fit leads to greater consistency than the T11 model with the counts measured by the Cosmic Background Imager (CBI) (Mason et al. 2003) and the Sunyaev-Zel’dovich Array (SZA) (Muciovej et al. 2010), but is in greater disagreement with the Green Bank Telescope (GBT) survey by Mason et al. (2009) (all of which were previously presented and compared in T11). The disagreement between our predictions and the GBT survey measurements might be explained in part by the lower resolution of 24 arcsec for the GBT survey as well as the targeted source selection from the NVSS. For all fluxes less than ~ 0.1 Jy our predicted counts are now larger than the de Zotti et al. (2005) model (shown by the dotted green line). Also

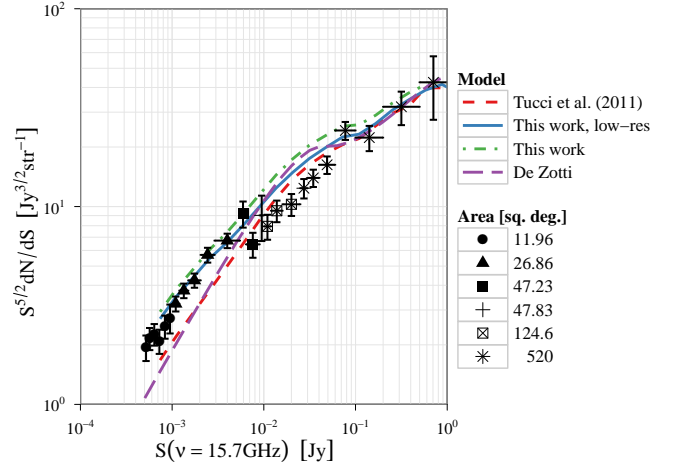


Figure 5. Comparison of our predicted counts at 15.7 GHz with those measured in the 9C and 10C surveys by AMI Consortium et al. (2011). The dash-dotted green line shows our model prediction while the solid blue line shows the same model prediction after merging sources to be consistent with the 30 arcsecond resolution of the 9C and 10C surveys. In both cases we draw sources from our fits to the 5 GHz counts and 1.4–5 GHz spectral index distributions and then extrapolate the fluxes to 15.7 GHz (before merging the sources for the solid blue line). The dashed red line instead uses the 5 GHz counts and index distribution fits provided in T11 (unfairly applied at fluxes lower than those considered in T11). The long-dashed purple line shows the model from de Zotti et al. (2005). The data points are from Table 6 of AMI Consortium et al. (2011) with Poisson error bars added.

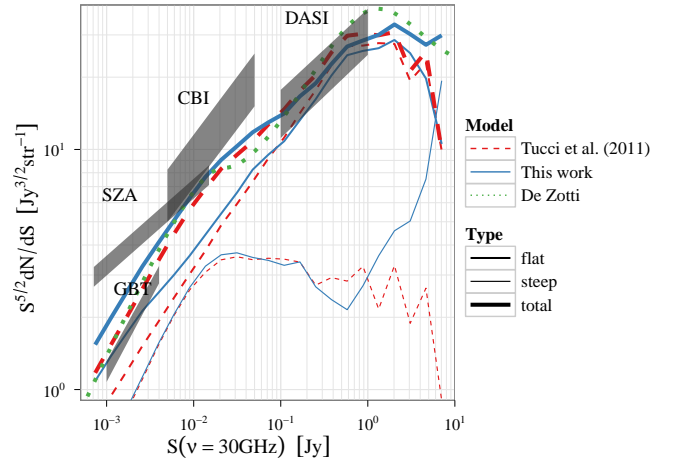


Figure 6. Predicted differential number counts at 30 GHz using the T11 SED model to extrapolate the modeled 5 GHz counts. The thin lines show the steep source counts (at the bottom of the figure), the slightly thicker lines show the flat+inverted counts, and the thickest lines show the sum of the steep and flat+inverted counts. The solid blue lines use our fits to the 5 GHz counts and 1.4–5 GHz spectral index distributions while the dashed red lines use those from T11 (as in Figure ??). The dotted green line is the model from de Zotti et al. (2005). The shaded bands showing measurements at 33 GHz are copied from Figure 12 in T11.

note that our predicted number counts are significantly larger than those of Colombo & Pierpaoli (2010) (their Figure 5) from a simulation based on the NVSS source catalog.

Finally, ACT (Marriage 2011) and SPT (Vieira et al.

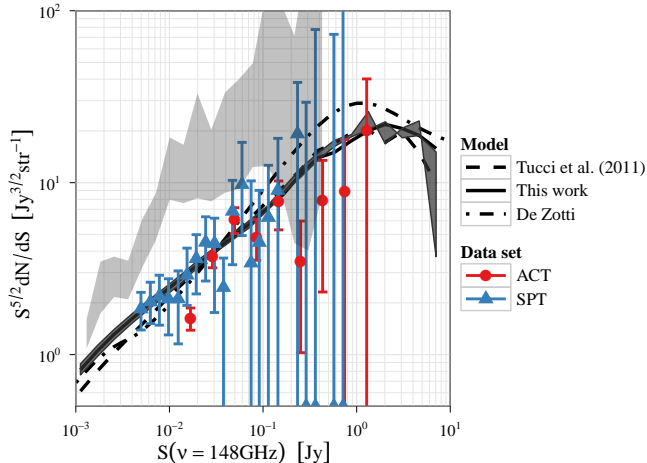


Figure 7. Predicted differential number counts at 148 GHz with the same models as in Figures ?? and 6. The dark gray shaded band denotes the range of extrapolated number count predictions when the faint slope, k_f , for the flat+inverted 5 GHz number counts is varied over its 68% confidence interval. The data points are taken from Marriage (2011) for ACT and Vieira et al. (2010) for SPT. The light gray shaded band shows the 95% confidence intervals for the number counts when each source flux in the NOAO DFS and ATESP catalogs is extrapolated using a power-law SED as described in Appendix A. The power-law SED band is intended to show the range of extrapolated count uncertainties when marginalizing over SED parameters given only the NOAO DFS and ATESP catalogs.

2010) have recently presented catalogs of resolved point sources at 148 GHz, which we compare with our model in Figure 7. Again, our model predicts larger number counts than the T11 and De Zotti models for fluxes less than ~ 50 mJy. The uncertainty in the predicted counts from the 68% uncertainty range in k_f is shown by the gray shaded band in Figure 7 and is much less than the difference between models for $S \lesssim 50$ mJy. All the models are consistent with the SPT measurements but the increased counts for faint fluxes predicted by our model is in tension with the lowest-flux ACT measurement. The model predictions at 148 GHz depend sensitively on the SED model parameters, in particular the flat-spectrum source break frequency distribution described in T11 and Section 3.2. So it is possible that the tension between our model prediction and the ACT measurement indicates that the break frequencies are really smaller than we have modeled for the flat-spectrum sources in our catalog with 5 GHz fluxes less than 10 mJy. However, the break frequencies are degenerate with the spectral indices after the break in the SED when comparing with high-frequency number counts so we cannot make unambiguous conclusions about the SED model from the comparison in Figure 7.

We have also plotted the 95% confidence intervals for the extrapolated number counts as a gray shaded band in Figure 7 assuming a PL SED model and using the error propagation methods described in Appendix A. The confidence intervals for the PL SED model include both uncertainties in the SED parameters and the Poisson uncertainties from the limited size of the NOAO DFS and ATESP catalogs (the PL SED predictions use only the NOAO DFS and ATESP catalogs as input). When ex-

Table 2
Predicted Poisson Power for Planck Lower-frequency Channels

Freq. (GHz)	S_{cut} (Jy)	C_ℓ Tucci (μK^2)	C_ℓ This Work (μK^2)
30	0.48	2.8E-02	2.7E-02
44	0.58	6.6E-03	6.2E-03
70	0.48	8.2E-04	7.7E-04
100	0.34	1.6E-04	1.5E-04
143	0.21	3.3E-05	3.2E-05
217	0.18	1.5E-05	1.5E-05

trapolating source fluxes over such a broad frequency range the PL SED is of course a poor model, but we include it in Figure 7 to demonstrate the expected modeling uncertainties for the flux extrapolation. A similar error propagation for all the SED parameters in the Tucci model could yield even larger uncertainties. But the Tucci SED model is calibrated against many other datasets so the priors on the SED parameters might limit the increase in the uncertainties relative to the PL SED model when all SED parameters are marginalized. We have left this investigation for future work.

4.2. CMB Power Spectrum

As shown in, e.g., Tegmark & Efstathiou (1996); Scott & White (1999) the Poisson contribution to the CMB power spectrum from unresolved point sources is

$$C_\ell(\nu) = g^2(\nu) \int_0^{S_{\text{cut}}} S_\nu^2 \frac{dN}{dS_\nu} dS_\nu, \quad (7)$$

where $g(\nu)$ converts from intensity at frequency ν to temperature in μK , and S_{cut} is the minimum flux (in a given channel) at which point sources can be resolved and masked out or otherwise removed. The same radio sources also contribute a clustering foreground to the CMB power spectrum, but this is expected to be sub-dominant to the Poisson power for the source intensities we are considering here (Scott & White 1999).

In Table 2 we evaluate Equation (7) for the lower frequency Planck channels using the S_{cut} values from the Early Release Compact Source catalog (ERCSC) given in Table 3 of Planck Collaboration et al. (2011). We have omitted predictions for the Poisson power for the three highest frequency Planck channels both because the unresolved radio sources become a sub-dominant foreground at those frequencies and because the flux extrapolation becomes increasingly unreliable.

We show similar predictions for the Poisson power for ACT and SPT in Table 3 assuming $S_{\text{cut}} = 0.005$ Jy for SPT (Vieira et al. 2010) and $S_{\text{cut}} = 0.02$ Jy for ACT (Marriage 2011).

We further compare the different model predictions for the Poisson power in Planck, ACT and SPT channels in Figure 8. Each panel shows the predicted Poisson power for our model and the De Zotti model, both normalized to the prediction from the T11 model as a functions of S_{cut} . The top six panels show the predictions for the six lowest-frequency Planck channels while the bottom two panels show predictions for the lower ACT and SPT frequencies and S_{cut} ranges. We have plotted only those frequency channels that have predicted radio source Poisson power

Table 3
Predicted Poisson Power for ACT and SPT

Freq. (GHz)	S_{cut} (Jy)	C_ℓ Tucci (μK^2)	C_ℓ This Work (μK^2)
95	0.005	2.5E-06	3.1E-06
148	0.005	6.1E-07	7.6E-07
148	0.02	2.7E-06	3.1E-06
217	0.005	3.2E-07	4.0E-07
217	0.02	1.5E-06	1.7E-06
277	0.02	1.6E-06	1.8E-06

much larger or comparable to the infrared source Poisson power as predicted by the model from Equation (4) of Millea et al. (2011) (using their amplitude normalized to Planck and SPT). We plot the predicted infrared source Poisson power with black crosses or arrows (when outside the scale of the panel) only where the prediction is comparable to or larger than the radio source Poisson power (i.e. the highest frequency panel for each S_{cut} range). The circular points and red lines in Figure 8 show the predictions using the mean of the marginal posterior for k_f from Equation (1) while the blue triangles and lines show the model from de Zotti et al. (2005). The red shaded bands show the range of predictions for k_f values spanning the 68% confidence intervals of the marginal posterior given the 5 GHz number count observations. The gray shaded bands are similar, but also include the variation of the 1.4–5 GHz spectral indices of the flat+inverted sources over their 68% confidence intervals as reported in Table 1. For Planck, our model predicts Poisson power that matches the prediction from the T11 model to within 10% for all S_{cut} values. This is because our data modify the T11 model at 5 GHz only for source fluxes $\lesssim 100$ mJy while the Planck Poisson power is mostly determined by sources with fluxes just below $S_{\text{cut}} > 100$ mJy. The De Zotti model predicts higher Poisson power than the T11 model and our model because of an excess of sources with fluxes just below S_{cut} . This is the reason for the different dependence on S_{cut} of the two models in the 70 and 100 GHz panels of Figure 8. At the ACT and SPT frequencies in the bottom 2 panels of Figure 8, our model predictions are consistently above both the De Zotti and T11 models, as also indicated in Figure 7. The excess faint sources in our catalogs predict increased Poisson power in ACT and SPT of 5%–30% relative to the T11 model, ignoring any uncertainties in the Tucci SED model parameters.

In Figure 9, we plot the different Poisson power model predictions in the four lowest-frequency Planck channels compared with the TT CMB power spectrum (predicted with Emu CMB Schneider et al. 2011) and the expected errors from the average noise per pixel and beam smearing. Figure 9 makes it clear that the Poisson contribution to the total observed power is comparable to or sub-dominant to the noise in each channel. While the resolution is better in higher-frequency Planck channels, the Poisson power from millimeter sources will dominate over the radio sources we are modeling. We also plot in Figure 9 the 95% confidence intervals on the predicted Poisson power assuming a PL SED derived using the methods in Appendix A. The sizes of the uncertainties for the PL SED are comparable to the variation in the

Table 4
Scalar Spectral Index Bias from Wrong Point-source Model with Four Low-frequency Planck Channels.

S_{cut} (Jy)	n_s Bias	n_s Bias/ $\sigma(n_s)$
0.6	0.0080	0.55
0.4	0.0071	0.49
0.2	0.0037	0.25

Poisson power for the range of S_{cut} values in the ERCSC and are much larger than the variation between the Tucci SED models for a fixed S_{cut} value.

We showed in the upper panels of Figure 8 that our 5 GHz number count measurements predict no more than 10% changes in the predicted radio source Poisson power in any Planck channel relative to earlier models. We now consider whether our data yield 5 GHz count measurements that provide a sufficient model to remove the bias in constraints on the scalar spectral index, n_s , from radio foregrounds in the Planck temperature power spectrum. We adopt the Fisher matrix formalism as described in Huterer & Takada (2005) to predict the bias on n_s assuming our model with the 5 GHz number count slope $k_f = 0.452$ (our $+1\sigma$ fit value) is the “truth,” but that our model with $k_f = 0.423$ (our -1σ fit value) is used to subtract the Poisson power when analyzing the data. For computing the Fisher matrix we use the power spectrum noise model including the Poisson contribution from White (1998) as well as the optimal linear estimator therein for the CMB power spectrum given the five lowest-frequency Planck channels. The inferred biases on n_s assuming the same S_{cut} value for each channel are shown in Table 4. The last column of the table also shows the biases normalized by the marginal Fisher matrix $1-\sigma$ uncertainties on n_s .

We marginalized over five other cosmological parameters (as in Schneider et al. 2011). For all S_{cut} values, the biases on n_s are smaller than the 1σ marginal Fisher errors. So, by this measure, the remaining uncertainties in the 5 GHz counts fit from our catalogs are not significant for Planck parameter estimation (neglecting uncertainties in the SED models).

5. DISCUSSION

We have shown that a previously unconsidered population of faint radio sources at 1.4 and 5 GHz with flat and inverted spectral indices could significantly contribute to the unresolved point source contamination in the power spectrum measurements in ongoing high resolution CMB experiments. However, the measured differential number counts of faint radio sources are not large enough to significantly modify previous predictions for the Poisson power in the Planck temperature power spectrum. Our source catalog is unique in the combination of flux sensitivity to 1.5 mJy, resolution of 5 arcsec, area covered of 7 deg^2 and matching of sources in the 1.4 and 5 GHz frequency bands.

We found that existing fits to the differential number counts of 5 GHz flat and inverted spectrum sources must have a shallower slope for fluxes less ~ 100 mJy in order to be consistent with our catalog. We also found that the distribution of 1.4–5 GHz spectral indices of sources with 5 GHz fluxes less than 100 mJy

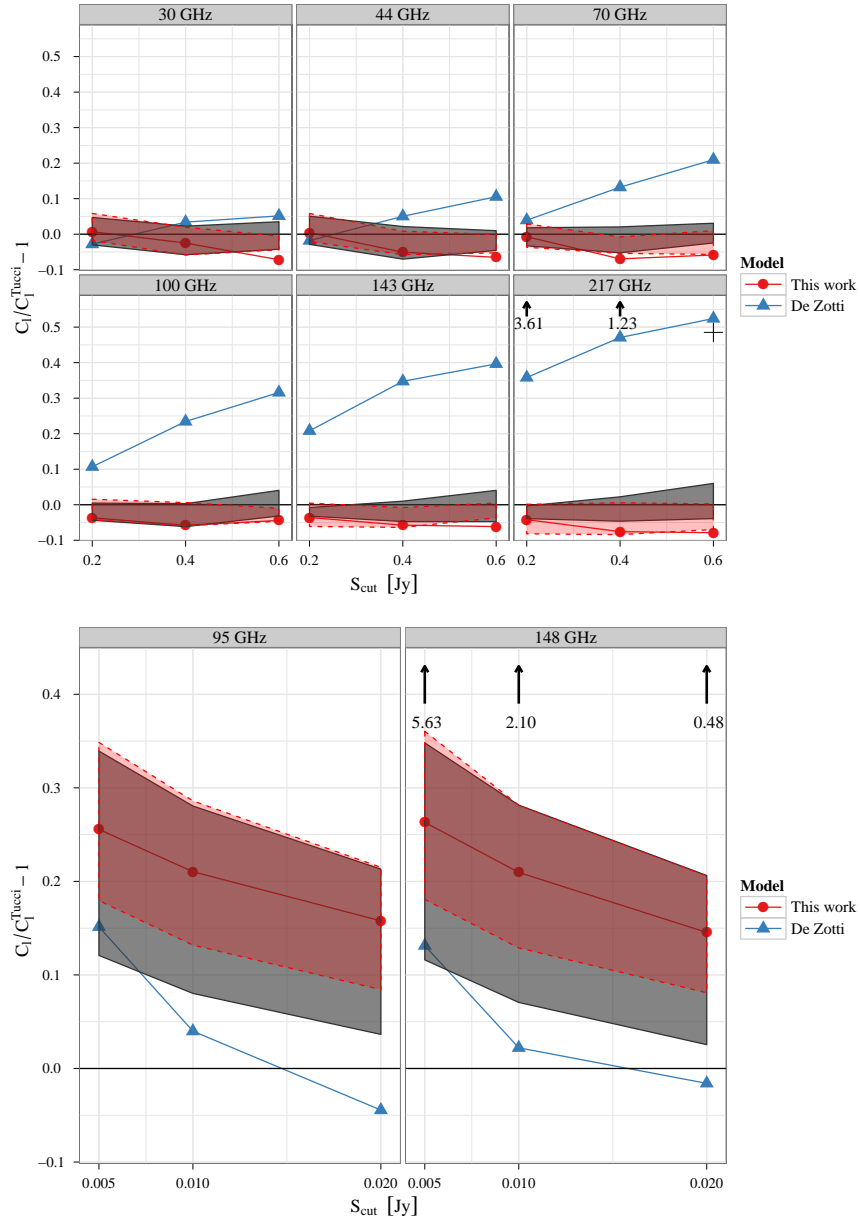


Figure 8. Predicted CMB Poisson power from unresolved radio point sources as a function of the minimum flux, S_{cut} , at which point sources can be resolved and excised. The model from this paper (“This work”) and the model from de Zotti et al. (2005) are shown by the red circles and blue triangles, respectively, normalized by the model from T11. The red shaded bands with the dashed outlines show the range of the predicted Poisson power when the flat+inverted 5 GHz differential number count slope k_f (see Equation (1)) is varied over its 68% confidence interval (when fit to our data and that in T11). The gray shaded bands show the range of predicted Poisson power including both the aforementioned variation in k_f as well as the variation of the 1.4–5 GHz spectral indices over the 68% conditional confidence intervals in the mean of the inverted spectral index distributions (see Figure 4 and Table 1). At frequencies where the Poisson power from infrared sources is comparable or larger than that from radio sources we have included either a black cross or black arrows (when the T11 normalized values do not fit within the plot range). In both the top and bottom panels, the millimeter source Poisson power dominates the radio source power for higher frequencies than those shown but is highly sub-dominant for all but the highest shown frequency panels.

is skewed toward larger values than the distributions for higher flux sources. Taken together these changes to the 5 GHz source counts imply increased differential counts when the fluxes are extrapolated to higher frequencies and therefore increases in the predicted level of Poisson power from unresolved point sources in CMB measurements.

The quantitative predictions of high-frequency number counts depend on the choice of SED model for extrapolating the measured 5 GHz fluxes. And the uncertainties in

the predicted high-frequency counts depend on the prior constraints on SED model parameters given a choice of SED model. Our main results assume a physically motivated SED model (from Tucci et al. 2011) but we also investigated a simple PL SED model to assess the dependence of our predictions on SED modeling uncertainties. In general we found that propagating the uncertainties from both the limited size of our catalog and two unknown SED model parameters can lead to high frequency prediction uncertainties that are much larger than the

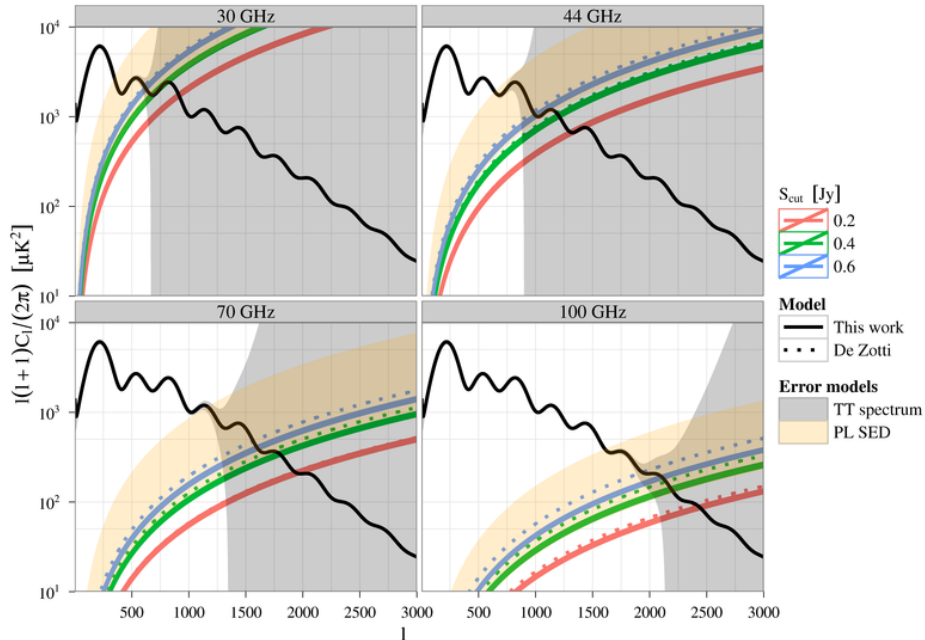


Figure 9. CMB power spectra in the four lowest-frequency Planck channels. The Poisson contribution to the power from unresolved point sources is shown for three different values of S_{cut} using both the updated 5 GHz number count model and spectral index distributions (“This work”) and the model from de Zotti et al. (2005). The line widths for our model (“This work”) denote the prediction range when k_f is varied over its 68% confidence interval. The T11 model predictions are always within the line widths of our model. The black line and gray shading show the TT CMB power spectrum and expected errors from pixel noise and beam smearing. The orange shaded band shows the 95% credible intervals for the Poisson contribution from the sources in the NOAO DFS catalog and assuming a power-law (“PL”) SED model with $S_{\text{cut}} = 0.4$ Jy.

differences between the predictions of competing SED models. However, we have argued that systematic offsets in the high-frequency predictions may persist even when the prediction uncertainties are large so that the predictions calibrated against our catalog will be important considerations for analyzing CMB experiments. As one example we find that if the four lowest-frequency Planck channels are optimally combined to constrain n_s from the CMB temperature power spectrum, the constraints are biased by less than the size of the 1σ uncertainties if the “wrong” point source number count model is used to subtract the Poisson power. We limited our forecasts in this example to the five lowest frequency Planck channels to avoid modeling other more dominant foregrounds at higher frequencies. So, our forecasts are simply an illustration of the significance of the difference between point source models rather than predictions of the optimal Planck constraints when all channels are considered, but we argue that our catalog shows that radio source models at 5 GHz are sufficient for removing Planck Poisson power as a systematic.

We outlined methods in Appendix A for propagating both measurement and SED model uncertainties when extrapolating fluxes on a source-by-source basis. A rigorous approach to predicting the Poisson power from unresolved point sources in CMB observations could apply the methods of Appendix A to a combined catalog of all available radio survey data at relevant frequencies. We expect that significant constraints on the uncertain SED model parameters could be imposed by such a joint analysis of available data, thereby removing a key uncertainty from the present work while also providing useful physi-

cal parameterizations of the radio Poisson foreground (as used in Paoletti et al. 2011). However, we leave this for future investigations.

ACKNOWLEDGMENTS

We thank Lloyd Knox, Marius Millea, and Mark Ammons for helpful comments on an early version of this draft and an anonymous referee for significant improvements. This work performed in part under the auspices of the U.S. Department of Energy by Lawrence Livermore National Laboratory under Contract DE-AC52-07NA27344. The National Radio Astronomy Observatory is a facility of the National Science Foundation operated under cooperative agreement by Associated Universities, Inc.

Facility: VLA.

APPENDIX

ERROR PROPAGATION FOR EXTRAPOLATED FLUXES

For a given SED model $\bar{S}(\nu, \theta)$ with parameters θ , we assume a log-normal likelihood for the observed fluxes of the i th object in the catalog. We choose a log-normal likelihood because it has strictly positive support and becomes nearly symmetric about the mean when the flux errors are small or the flux is large.

To propagate our uncertainty in the measured fluxes and SED parameters to the extrapolated fluxes, we compute the marginal posterior distribution for the extrapolated flux,

$$P(S_\nu | \hat{S}_i) = \int d\theta P(S_\nu | \theta) P(\theta | \hat{S}_i). \quad (\text{A1})$$

The first term gives a delta function, $P(S_\nu|\boldsymbol{\theta}) = \delta_D(S_\nu - \bar{S}(\nu, \boldsymbol{\theta}))$, which fixes one of the SED parameters as a function of the remaining SED parameters and the given value of S_ν . For a PL SED, the delta function effectively sets $\alpha = \ln\left(\frac{S_\nu}{S_0}\right) / \ln\left(\frac{\nu}{\nu_0}\right)$ (or $S_0 = S_0(S_\nu, \alpha)$). The marginalization in Equation (A1) then becomes

$$P(S_\nu|\hat{S}_i) \propto \frac{1}{S_\nu \ln(\nu/\nu_0)} \int dS_0 P(\hat{S}_i|S_0, \alpha(S_0, S_\nu)) P(S_0), \quad (\text{A2})$$

where the coefficient in front of the integral comes from the transformation of variables in the delta function. We assume a conjugate log-normal prior for S_0 with mean μ_{S_0} and standard deviation σ_{S_0} .

Performing the integration over S_0 , the final expression for the marginal posterior for the extrapolated flux of an individual source for a PL SED is

$$P(S_\nu|\hat{S}_i) = \frac{1}{A_{S_\nu}} S_\nu^{\alpha_{S_\nu}} \exp\left[-\frac{1}{2} \frac{(\ln(S_\nu) - \mu_{S_\nu})^2}{\sigma_{S_\nu}^2}\right], \quad (\text{A3})$$

where, if we assume $\nu_0 = 1.4$ GHz,

$$x_5 \equiv \frac{\ln(5/\nu_0)}{\ln(\nu/\nu_0)}, \quad (\text{A4})$$

and with $\sigma_{1,5} \equiv \sigma_{S_{1.4,5}}/S_{1.4,5}$,

$$\mu_{S_\nu} \equiv x_5 \frac{(\sigma_{S_0}^2 + \sigma_1^2) \ln(S_5) + (x_5 - 1) \sigma_{S_0}^2 \ln(S_1)}{x_5^2 (\sigma_{S_0}^2 + \sigma_1^2)}, \quad (\text{A5})$$

$$\sigma_{S_\nu} \equiv \frac{\sigma_1^2 \sigma_5^2 + \sigma_{S_0}^2 ((x_5 - 1)^2 \sigma_1^2 + \sigma_5^2)}{x_5^2 (\sigma_{S_0}^2 + \sigma_1^2)}, \quad (\text{A6})$$

$$\alpha_{S_\nu} \equiv -1 + \frac{\mu_{S_0} (x_5 - 1) x_5 \sigma_1^2}{\sigma_1^2 \sigma_5^2 + \sigma_{S_0}^2 ((x_5 - 1)^2 \sigma_1^2 + \sigma_5^2)}, \quad (\text{A7})$$

and,

$$A_{S_\nu} \equiv \sqrt{2\pi\sigma_{S_\nu}^2} \exp\left[\frac{1}{2}(1 + \alpha_{S_\nu})^2 2\mu_{S_\nu} + (1 + \alpha_{S_\nu})\sigma_{S_\nu}^2\right]. \quad (\text{A8})$$

We then estimate the mean differential number counts by summing over the (normalized) posteriors in bins in flux,

$$\begin{aligned} \frac{dN_k(> S)}{dS} \Delta S_k &\approx \sum_{i=1}^{N_{\text{sources}}} \int_{S_{\min,k}}^{S_{\max,k}} dS P(S_\nu|\hat{S}_i) \\ &\equiv \sum_{i=1}^{N_{\text{sources}}} p_{ik}, \end{aligned} \quad (\text{A9})$$

where $\Delta S_k \equiv S_{\max,k} - S_{\min,k}$ and $k = 1, \dots, N_{\text{bins}}$ index bins in S .

The Poisson contribution to the CMB power spectrum

Table 5

Random Sub-sample of the Catalogue of Matched Sources in the NOAO DFS.

R.A. (deg.)	Decl. (deg.)	S_5 (mJy)	$\sigma(S_5)$ (mJy)	$S_{1.4}$ (mJy)	$\sigma(S_{1.4})$ (mJy)	$\alpha_{1.4-5}$
34.01473	-5.13245	6.01	0.26	20.43	0.15	-0.96
30.99103	-4.96195	3.62	0.29	7.91	0.14	-0.61
30.86276	-4.98161	3.90	0.27	7.30	0.15	-0.49
33.28917	-4.09886	0.98	0.35	6.11	0.14	-1.44
33.34937	-4.33320	13.54	0.38	65.49	0.17	-1.24
33.88087	-4.68231	3.92	0.46	7.18	0.15	-0.48
31.76899	-3.81961	10.64	0.30	34.55	0.15	-0.93
33.44730	-3.71314	10.47	0.30	33.00	0.14	-0.90
33.56511	-5.52509	3.39	0.58	4.84	0.15	-0.28
31.06313	-4.72039	11.24	0.30	30.47	0.17	-0.78
33.19339	-3.61151	1.97	0.49	18.54	0.15	-1.76
32.27030	-5.10399	1.07	0.28	4.04	0.14	-1.04
31.32263	-5.27310	1.69	0.38	2.24	0.16	-0.22
32.76205	-4.89393	4.67	0.36	2.12	0.15	0.62
34.04510	-4.43530	21.66	0.28	23.80	0.15	-0.07

can be written as,

$$\begin{aligned} C_\ell(\nu) &= \sum_{i=1}^{N_{\text{sources}}} \int_0^{S_{\text{cut}}} dS S^2 P(S_\nu|\hat{S}_i) \\ &= \sum_{i=1}^{N_{\text{sources}}} \\ &\quad \times \sqrt{\frac{\pi}{2}} \frac{\sigma_{S_\nu}}{A_{S_\nu}} \exp\left[\frac{1}{2}(\alpha_{S_\nu} + 3)((\alpha_{S_\nu} + 3)\sigma_{S_\nu}^2 + 2\mu_{S_\nu})\right] \\ &\quad \times \left(1 - \text{Erf}\left[\frac{(\alpha_{S_\nu} + 3)\sigma_{S_\nu}^2 + \mu_{S_\nu} - \ln(S_{\text{cut}})}{\sqrt{2}\sigma_{S_\nu}^2}\right]\right), \end{aligned} \quad (\text{A10})$$

where the index i in the final equality is implicit in all the flux posterior parameters and ‘‘Erf’’ denotes the error function.

NOAO DFS CATALOGUE

A random sub-sample of the catalog of 362 sources in the NOAO DFS matched at 1.4 and 5 GHz is shown in Table 5. The spectral index values in the final column are derived from Columns 3 and 5 via the relation $\alpha_{1.4-5} \equiv \log(S_5/S_{1.4}) / \log(5/1.4)$. The full catalog is available for download from the VizieR database.

REFERENCES

- AMI Consortium, Davies, M. L., Franzen, T. M. O., Waldram, E. M., Grainge, K. J. B., Hobson, M. P., Hurley-Walker, N., Lasenby, A., Olamaie, M., Pooley, G. G., Riley, J. M., Rodríguez-González, C., Saunders, R. D. E., Scaife, A. M. M., Schammel, M. P., Scott, P. F., Shimwell, T. W., Titterton, D. J., & Zwart, J. T. L. 2011, MNRAS, 415, 2708
 Colombo, L. P. L. & Pierpaoli, E. 2010, MNRAS, 407, 247
 Curto, A., Martínez-González, E., Barreiro, R. B., & Hobson, M. P. 2011, MNRAS, 417, 488
 Danese, L., Franceschini, A., Toffolatti, L., & de Zotti, G. 1987, ApJ, 318, L15
 de Zotti, G., Massardi, M., Negrello, M., & Wall, J. 2010, The A&A Review, 18, 1
 de Zotti, G., Ricci, R., Mesa, D., Silva, L., Mazzotta, P., Toffolatti, L., & González-Nuevo, J. 2005, A&A, 431, 893
 Elsner, F., Wandelt, B. D., & Schneider, M. D. 2010, A&A, 513, A59

- Guerra, E. J., Newlander, S. M., Haarsma, D. B., & Bruce Partridge, R. 2002, *New Astron. Rev.*, 46, 303
- Hogg, D. W. 2008, arXiv.org, 0807, 4820
- Huffenberger, K. M., Eriksen, H. K., Hansen, F. K., Banday, A. J., & Górski, K. M. 2008, *ApJ*, 688, 1
- Huterer, D. & Takada, M. 2005, *Astropart. Phys.*, 23, 369
- Knox, L. 1999, *MNRAS*, 307, 977
- Knox, L., Holder, G. P., & Church, S. E. 2004, *ApJ*, 612, 96
- Lin, Y.-T., Partridge, B., Pober, J. C., Boucheffy, K. E., Burke, S., Klein, J. N., Coish, J. W., & Huffenberger, K. M. 2009, *ApJ*, 694, 992
- Marriage, T. A. e. a. 2011, *ApJ*, 731, 100
- Mason, B. S., Pearson, T. J., Readhead, A. C. S., Shepherd, M. C., Sievers, J., Udomprasert, P. S., Cartwright, J. K., Farmer, A. J., Padin, S., Myers, S. T., Bond, J. R., Contaldi, C. R., Pen, U., Prunet, S., Pogosyan, D., Carlstrom, J. E., Kovac, J., Leitch, E. M., Pryke, C., Halverson, N. W., Holzzapfel, W. L., Altamirano, P., Bronfman, L., Casassus, S., May, J., & Joy, M. 2003, *ApJ*, 591, 540
- Mason, B. S., Weintraub, L., Sievers, J., Bond, J. R., Myers, S. T., Pearson, T. J., Readhead, A. C. S., & Shepherd, M. C. 2009, *ApJ*, 704, 1433
- Millea, M., Doré, O., Dudley, J., Holder, G., Knox, L., Shaw, L., Song, Y.-S., & Zahn, O. 2011, arXiv, 1102, 5195
- Muchovej, S., Leitch, E., Carlstrom, J. E., Culverhouse, T., Greer, C., Hawkins, D., Hennessy, R., Joy, M., Lamb, J., Loh, M., Marrone, D. P., Miller, A., Mroczkowski, T., Pryke, C., Sharp, M., & Woody, D. 2010, *ApJ*, 716, 521
- Paoletti, D., Aghanim, N., Douspis, M., Finelli, F., De Zotti, G., Lagache, G., & Pénin, A. 2011, arXiv:1112.3260
- Perna, R. & Di Matteo, T. 2000, *ApJ*, 542, 68
- Pierpaoli, E. & Perna, R. 2004, *MNRAS*, 354, 1005
- Planck Collaboration, Ade, P. A. R., Aghanim, N., Arnaud, M., Ashdown, M., Aumont, J., Baccigalupi, C., Balbi, A., Banday, A. J., Barreiro, R. B., & et al. 2011, *A&A*, 536, A7
- Prandoni, I., de Ruiter, H. R., Ricci, R., Parma, P., Gregorini, L., & Ekers, R. D. 2010, *A&A*, 510, A42
- Prandoni, I., Gregorini, L., Parma, P., de Ruiter, H. R., Vettolani, G., Wieringa, M. H., & Ekers, R. D. 2000, *A&AS*, 146, 41
- Prandoni, I., Parma, P., Wieringa, M., de Ruiter, H. R., Gregorini, L., Mignano, A., Vettolani, G., & Ekers, R. D. 2006, *A&A*, 457, 517
- Rani, B., Gupta, A. C., Bachev, R., Strigachev, A., Semkov, E., D'Ammando, F., Wiita, P. J., Gurwell, M. A., Ovcharov, E., Mihov, B., Boeva, S., & Peneva, S. 2011, *MNRAS*, 417, 1881
- Reese, E. D., Mroczkowski, T., Menanteau, F., Hilton, M., Sievers, J., Aguirre, P., Appel, J. W., Baker, A. J., Bond, J. R., Das, S., Devlin, M. J., Dicker, S. R., Dunner, R., Essinger-Hileman, T., Fowler, J. W., Hajian, A., Halpern, M., Hasselfield, M., Hill, J. C., Hincks, A. D., Huffenberger, K. M., Hughes, J. P., Irwin, K. D., Klein, J., Kosowsky, A., Lin, Y.-T., Marriage, T. A., Marsden, D., Moodley, K., Niemack, M. D., Nolta, M. R., Page, L. A., Parker, L., Partridge, B., Rojas, F., Sehgal, N., Sifon, C., Spergel, D. N., Staggs, S. T., Swetz, D. S., Switzer, E. R., Thornton, R., Trac, H., & Wollack, E. J. 2011, arXiv:1108.3343
- Schneider, M. D., Holm, O., & Knox, L. 2011, *ApJ*, 728, 137
- Scott, D. & White, M. 1999, *A&A*, 346, 1
- Sehgal, N., Bode, P., Das, S., Hernandez-Monteagudo, C., Huffenberger, K., Lin, Y.-T., Ostriker, J. P., & Trac, H. 2010, *ApJ*, 709, 920
- Tegmark, M. & Efstathiou, G. 1996, *MNRAS*, 281, 1297
- Toffolatti, L., Argüeso Gomez, F., de Zotti, G., Mazzei, P., Franceschini, A., Danese, L., & Burigana, C. 1998, *MNRAS*, 297, 117
- Toffolatti, L., Negrello, M., González-Nuevo, J., de Zotti, G., Silva, L., Granato, G. L., & Argüeso, F. 2005, *A&A*, 438, 475
- Tucci, M., Toffolatti, L., de Zotti, G., & Martínez-González, E. 2011, *A&A*, 533, A57
- Vieira, J. D., Crawford, T. M., Switzer, E. R., Ade, P. A. R., Aird, K. A., Ashby, M. L. N., Benson, B. A., Bleem, L. E., Brodwin, M., Carlstrom, J. E., Chang, C. L., Cho, H. M., Crites, A. T., de Haan, T., Dobbs, M. A., Everett, W., George, E. M., Gladders, M., Hall, N. R., Halverson, N. W., High, F. W., Holder, G. P., Holzzapfel, W. L., Hrubes, J. D., Joy, M., Keisler, R., Knox, L., Lee, A. T., Leitch, E. M., Lucker, M., Marrone, D. P., McIntyre, V., McMahan, J. J., Mehl, J., Meyer, S. S., Mohr, J. J., Montroy, T. E., Padin, S., Plagge, T., Pryke, C., Reichardt, C. L., Ruhl, J. E., Schaffer, K. K., Shaw, L., Shirokoff, E., Spieler, H. G., Stalder, B., Staniszewski, Z., Stark, A. A., Vanderlinde, K., Walsh, W., Williamson, R., Yang, Y., Zahn, O., & Zenteno, A. 2010, *ApJ*, 719, 763
- White, M. 1998, *Phys. Rev. D(Particles)*, 57, 5273
- White, M. & Majumdar, S. 2004, *ApJ*, 602, 565
- White, R. L., Becker, R. H., Helfand, D. J., & Gregg, M. D. 1997, *ApJ*, 475, 479